HIGH RESOLUTION HYDROGEOPHYSICAL IMAGING AND CHARETERISATION

J. van der Kruk[1], A. Klotzsche[1], F. Lavoué[1], G.A. Meles[2], A. Mester[1], R.W. Jacob[3], J.A. Doetsch[2], N. Linde[4], H. Maurer[2], A.G. Green[2] and H. Vereecken[1]

[1] Research Center Jülich, Germany, j.van.der.kruk@fz-juelich.de

[2] ETH Zürich, Switzerland, meles@aug.ig.erdw.ethz.ch

[3] Bucknell University, U.S.A., rob.jacob@bucknell.edu

[4] University Lausanne, Switzerland, Niklas.Linde@unil.ch

ABSTRACT

Geophysical methods are important tools for a wide range of geological, hydrogeological, and engineering investigations. Conventional processing techniques for electromagnetic tools often use approximations that may be either inappropriate or only provide limited resolution. Higher resolution images can be derived by using more sophisticated approaches that explicitly take into account the electromagnetic wave propagation characteristics. Here, three relatively new developments to obtain high resolution images of quantitative medium properties are discussed: 1) electromagnetic induction (EMI) calibration using apparent electrical conductivity modeling based on electrical resistivity tomography, 2) dispersion inversion of ground-penetrating radar (GPR) data recorded across surface waveguides, and 3) full-wavefield inversion of crosshole tomographic GPR data.

Keywords: *Ground Penetrating Radar (GPR), Electromagnetic Induction (EMI), Inversion, Full-waveform, Waveguide, Dispersion*

1. INTRODUCTION

Electromagnetic parameters of the subsurface such as electrical conductivity and relative permittivity are of great interest for non-destructive determination of soil properties (e.g., clay content) or hydrologic state variables (e.g., soil water content). In the past decade, several non-invasive geophysical methods have been applied to measure subsurface parameters in situ. Here, we discuss the EMI and GPR geophysical methods and describe recently developed methods that improve the resolution and the quantitative information obtained from these data.

EMI appears to be an efficient method to cover large areas in a short time. However, this method currently does not provide absolute values of electrical conductivity due to calibration problems, which hinders a quantitative analysis of the measurement. In this study, we present a calibration method of EMI measurements with electrical conductivity values measured with electrical resistivity tomography (ERT).

Inversion of dispersed GPR data measured over low-velocity or leaky waveguides cannot be analyzed using standard ray-based techniques due to the interference of the multiple reflections within the waveguide. An inversion scheme similar to seismic Rayleigh and Love wave inversion was recently introduced that consists of calculating phase-velocity spectra, picking dispersion curves, and then inverting for the subsurface material

properties by explicitly taking into account the electromagnetic reflection and propagation characteristics. GPR data measured over a precipitation-induced waveguide shows clear dispersion and is inverted for the medium properties. The results correspond well with soil core analyses.

Conventional crosshole tomograms provided by standard ray-based methods have limited resolution, primarily because only a fraction of the information contained in the radar data is included in the inversion. Higher resolution radar tomograms can be derived by using full-waveform inversion schemes that take into account much of the recorded trace. Recently, a new full-waveform inversion scheme was developed that simultaneously updates the permittivity and conductivity distributions, exploits the full vector wavefield, and is able to invert crosshole and borehole-to-surface data sets jointly. Full-waveform inversion of experimental data acquired within a gravel deposit returns significantly higher resolution images than standard ray-based inversions.

2. ELECTROMAGNETIC INDUCTION CALIBRATION USING APPARENT ELECTRICAL CONDUCTIVITY MODELLING BASED ON ELECTRICAL RESISTIVITY TOMOGRAPHY

EM induction measures an apparent electrical conductivity at the surface, which represents a weighted average of the electrical conductivity distribution over a certain depth range (McNeill [1]), whereas ERT inversion can provide absolute values for local conductivities as a function of depth, which can be converted to water content using an empirical relationship (e.g. Archie's Law [2]). EM induction and ERT measurements were collected along a 120-metre-long transect with moderate lateral and vertical variation in electrical conductivity (Lavoué et al. [3]). To reconstruct the apparent electrical conductivity measured with EM induction, the inverted ERT data were used as input in an electromagnetic forward modeling tool for magnetic dipoles over a horizontally layered medium considering the frequencies and offsets used by the EM induction instruments. Comparison of the calculated and measured apparent electrical conductivities shows very similar trends but a shift in absolute values, which is attributed to system calibration problems (Triantafilis et al. [4], Sudduth et al. [5], Abdu et al. [6]; Gebbers et al. [7]). The measured apparent conductivities are plotted against the EM-based modeled apparent conductivities in Fig. 1 for the profiler (8 kHz and 15 kHz) and EM38 in both the horizontal coplanar (HCP) and vertical coplanar (VCP) configurations. In all cases, the HCP and VCP results do not match the 1:1 (dashed) line. All VCP measurements underestimate the EM-based apparent electrical conductivity. This indicates the need for a calibration of EM induction measurements., which can be performed by correcting the observed shift using a linear regression (Lavoué et al. [3]). The obtained apparent conductivity results are compared to the modelled EM-based data in Fig. 2. After calibration, the variations of the electrical conductivity along the transect for the measured and modeled data agree very well. Reliable quantitative values are vital for making a multi-layered inversion using HCP and VCP measurements possible. Any static shift will have a dramatic influence on the inversion results. Quantitative EM induction values and the possibility of acquiring EM induction data on large-scales offer great potential for a wide range of applications.

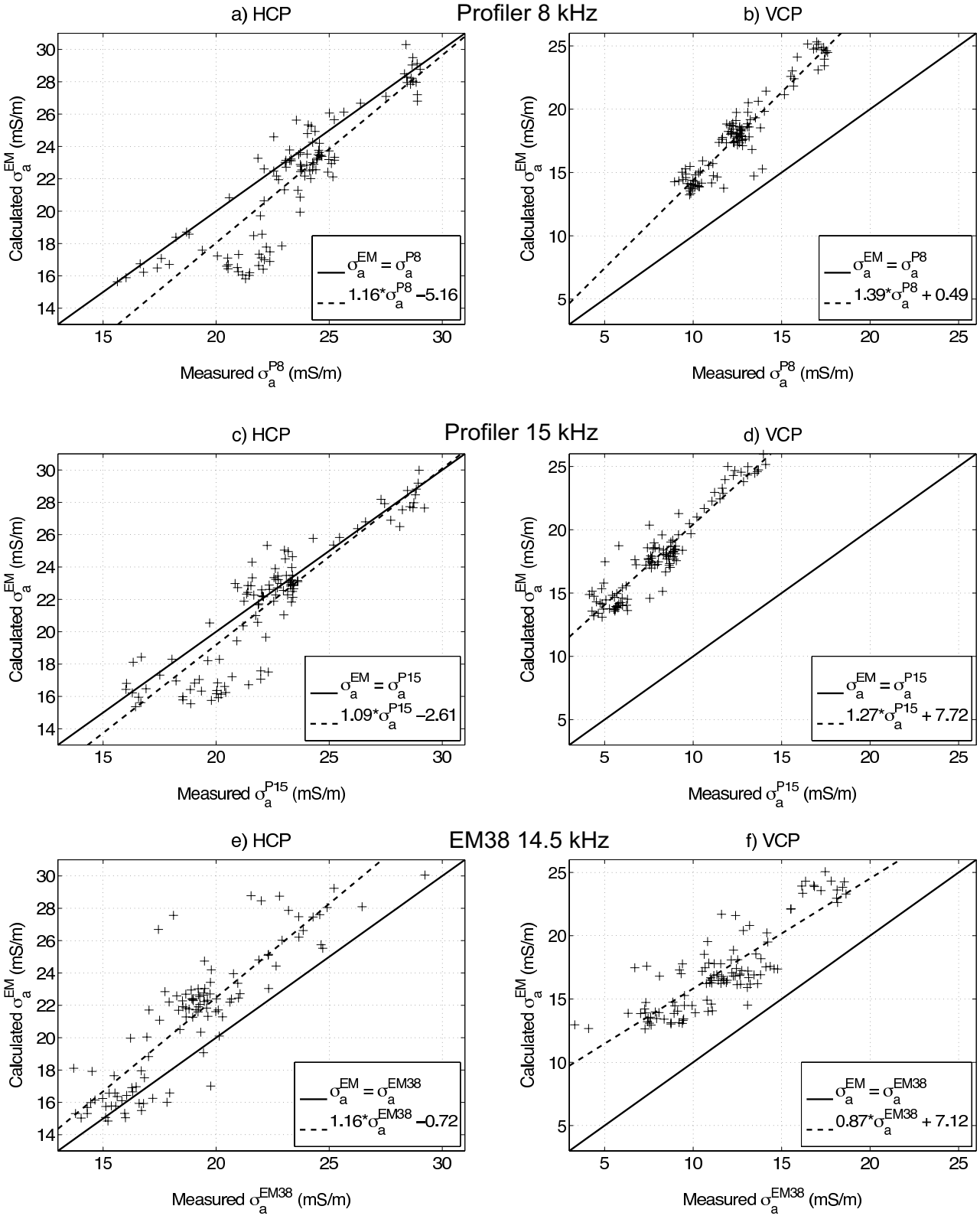

Fig. 1 HCP and VCP scatter plots of measured σ_a versus synthetic σ_a for profiler 8 kHz (a,b) and 15 kHz (c, d) and EM38 (e, f), respectively. Dashed lines show the corresponding linear regressions. After Lavoué et al., 2010 [3].

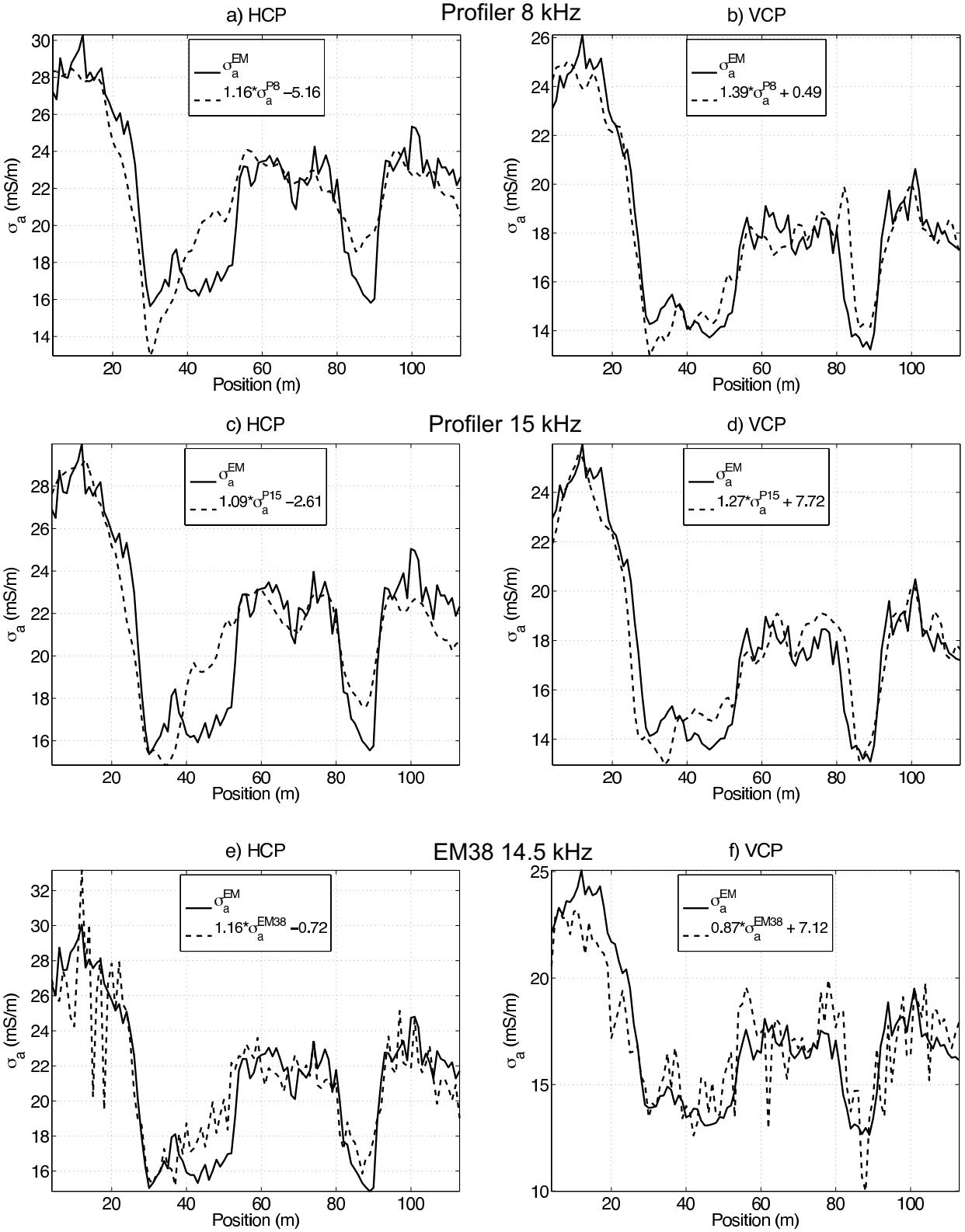

Fig. 2 HCP and VCP EM-based calculated apparent conductivities (black) and calibrated values from measured apparent conductivities (dashed line) for profiler 8 (a, b) and 15 (c, d) kHz and EM38 (e, f), respectively. After Lavoué et al., 2010 [3].

3. DISPERSION INVERSION OF GPR DATA RECORDED ACROSS SURFACE WAVEGUIDES

At locations where a thin surface layer overlies a substrate medium that has a lower permittivity, or a much larger permittivity/conductivity than the surface layer (Figure 3), pronounced dispersion of GPR waves can be observed and the surface layer acts as a waveguide. In both cases, the electromagnetic waves are trapped within the waveguide and the radar energy is internally reflected, resulting in a series of interfering multiples that manifest themselves as a package of dispersed waves that can propagate over large distances. Since these waveguides often have a thickness of the order of one wavelength, standard travel-time analysis of reflected waves cannot be reliably used to estimate the subsurface properties (van der Kruk et al., [8]), and specific inversion techniques should be used. Recently, techniques for inverting dispersive GPR data have been developed. They provide information on the thickness and permittivity of a single-layer waveguide and the permittivity of the underlying halfspace (van der Kruk, [9]; van der Kruk et al. [10]). More and more data sets are being identified as containing dispersive waves due to the presence of waveguides: a layer of wet, organic silty to gravelly soil overlying a drier layer of sand and gravel (Arcone et al. [11], Liu et al. [12]), an organic-rich sandy silt overlying gravel units (van der Kruk, [9], van der Kruk et al, [10]), a mountain slope with a 1-m soil cover (Strobbia and Cassiani, [13]), and thawing of a frozen soil layer (van der Kruk et al., [14]), an ice layer overlying water (Arcone, [11], van der Kruk, [15]), and the freezing of wet soil (van der Kruk et al., [14], Steelman et al., [16]).

We used a Sensors and Software PulseEKKO IV GPR system employing 200 MHz bi-static antennas to collect the GPR data. Two different source-receiver antenna configurations were used to collect the GPR data; broadside and endfire. The data collected in broadside and endfire configurations are called transverse electric (TE) and transverse magnetic (TM), respectively, referring to the orientation of either the electric field vector or the magnetic field vector with respect to the plane of incidence. Figures 4a and b show the TE and TM data measured after 72 mm rainfall over a dry sandy soil. The data, normalized on the maximum of each trace, show that the dispersive waves enclosed in the dotted lines contain most of the energy in the CMP data. The dispersive signal is identified by the shingled reflections present in the data. The dashed arrows indicate the apparent phase velocities of these shingling events, whereas the dotted arrows in Figure 4a and b indicate the group velocities. Note that there is a clear difference between the phase and group velocities which indicates a frequency dependent phase velocity. These properties are characteristic of dispersed GPR signals in CMP soundings (van der Kruk et al., [8]).
The phase-velocity spectra of the TE and TM data are shown in Figures 4c and d, respectively. Here, the fundamental TE_0 and TM_0 modes show clear dispersion. Dispersion curves are obtained by picking the maxima in the phase-velocity spectra, which are inverted for subsurface properties using a combined global- and local-minimization procedure.

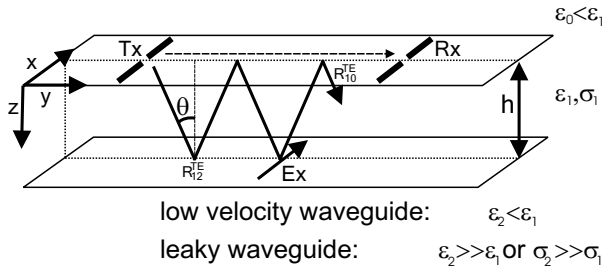

Fig. 3 Diagram of the broadside (TE) source-receiver

Diagram of the broadside (TE) source-receiver configuration.

TABLE 1 Model parameters of the global minima for the waveguide inversion of the data measured after 72 mm rainfall over a dry surface shown in Figures 2a-d.

Inversion	ε_1	ε_2	h (m)
TE_0	11.62	4.87	0.42
TM_0	9.77	4.53	0.54
TE_0TM_0	11.89	4.80	0.41

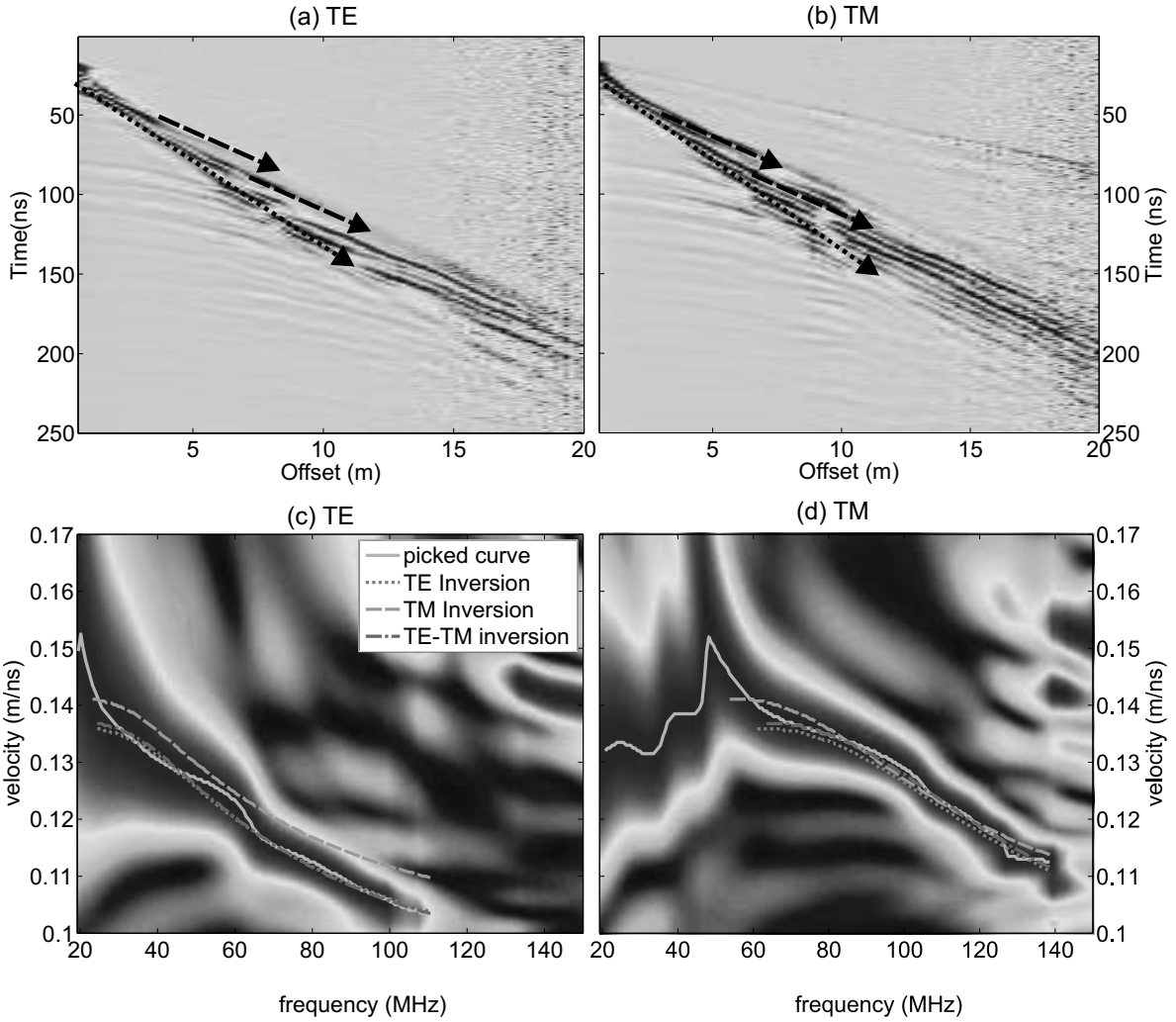

Fig.4 (a) TE and (b) TM CMP profiles measured after 72 mm rainfall over a dry sandy soil. The data are normalized to the maximum of each trace. The dotted arrow is the phase velocity, indicating the velocity with which the phases are traveling through the waveguide. Observed phase velocities are indicated by the dashed arrows. Corresponding (c) TE and (d) TM phase velocity spectra diagram of the broadside (TE) and endfire (TM) source-receiver setups, respectively.

Separate TE_0 and TM_0 inversions and a joint TE_0TM_0 inversion (van der Kruk et al., [9], van der Kruk, [10]) were carried out using the dispersion curves displayed in Figures 3c and d and the inversion results are given in Table 1. For comparison purposes, the computed TE_0 and TM_0 dispersion curves for the models determined from the two independent inversions and the joint inversion are plotted on the TE and TM phase-velocity spectra of Figures 4c and d. By combining the information contained in the two data sets in a joint TE_0TM_0 inversion, a single model is derived that fits both data sets. On the same date of GPR data collection (following the 72 mm of rainfall), a soil core of only 0.51 m was recovered (the remaining soil core was observed to fall out due to lack of cohesion). The relative permittivity of the upper 0.38 m was 8.55 and for the next 0.13 m was 4.46. The agreement in relative permittivity of the ε_2 from waveguide inversion and measured from soil core gives us confidence in the dispersion analysis. The obtained relative permittivity values can be converted to water content using Topp's equation [17]. Multi-layer inversion of dispersive GPR data are described by van der Kruk et al. [18].

4. SIMULTANEOUS FULL-WAVERFORM INVERSION OF CROSSHOLE TOMOGRAPHIC GPR DATA

Conventional GPR tomographic inversion, based on ray-based methods has limited resolution, primarily because only a fraction of the information contained in the radar data (i.e. the first-arrival times and maximum first-cycle amplitudes) is included in the inversion. Higher resolution radar tomograms can be derived by using full-waveform inversion schemes that take into account much more of the recorded trace. Full-waveform inversion is fairly advanced in exploration seismics (e.g. Tarantola, [19]; Mora, [20]; Maurer et al. [21]), whereas in GPR it is still under development (e.g. Ernst et al. [22, 23]). Seismic full-waveform inversion cannot be used for GPR inversion since the pertaining vectorial wave propagation and radiation patterns are completely different. Recently, a new inversion scheme was developed (Meles et al. [24]) that is based on a vectorial approach, which enables the joint inversion of crosshole and borehole-to-surface data sets. In addition, the new inversion scheme simultaneously updates the permittivity and conductivity using improved gradient and step length formulations (Meles et al. [24]). Synthetic analyses have shown that full-waveform tomographic imaging is able to accurately reconstruct the locations, sizes, and electrical properties of isolated and adjacent subwavelength objects embedded in homogeneous media. In addition, abrupt media boundaries and average and stochastic electrical property variations of heterogeneous layered models were accurately reconstructed (Ernst et al., [22]; Meles et al. [24]).

The full-waveform inversion scheme is based on a conjugate-gradient-type iterative scheme (Ernst et al, [22-23]) that requires (1) computation of the misfit between the observed and the computed traces, (2) back-propagation of the misfit in order to compute the gradient direction, (3) calculation of an optimal step length, and (4) update of the model according to the conjugate gradients at each iteration. By considering the vectorial nature of the electric fields and basing the inversion scheme on Maxwell's equations, the gradient in step (2) can be found by zero-lag cross-correlating both the vertical and horizontal components of these fields (Meles et al. [24]). This enables the possibility to also jointly invert crosshole and borehole-to-surface data. In addition, simultaneous updating of the permittivity and conductivity values was implemented in step (3), which resulted in faster convergence and more reliable results than sequential updating of permittivity and conductivity.
Experimental crosshole GPR data was acquired within a gravel aquifer in Switzerland (Klotzsche et al., [25]). Figure 5 shows a simplified geological representation of the investigation site. A limited number of transmitter positions were used during the data acquisition and a much larger number of receiver positions were occupied to minimize acquisition time and computational costs. Vertical spacings of 0.5m and 0.1m for the transmitter and receiver points were chosen, respectively. To avoid low coverage close to the transmitter borehole, sources and receivers were placed in either borehole. Ray-based permittivity and conductivity inversion results are shown in Figure 6a and c, respectively. The crosses and circles in Figure 6 indicate transmitter and receiver positions. Both permittivity and conductivity (logarithmic scale) images reveal roughly 3 zones. A zone of higher permittivity and higher electrical conductivity is found in the top 4 - 5.5m, followed by lower permittivity and lower conductivity values between 5.5 and 8m. The bottom part exhibits intermediate values for both parameters. Comparison of the measured data with synthetic data based on ray-based inversion results using FDTD modeling is shown in Figure 7a. Only a small area with a reasonable data fit is found as indicated by the ellipse. The final permittivity and conductivity result of the full-waveform inversion is presented in Figures 6b and 6d. They show much more detail than the ray-based inversion results in Figures 6a and 6c. Figure 7b compares the observed and modeled traces for transmitter position 7 after 35 iterations. A remarkably good fit between the synthetic and measured traces is apparent for the phase and amplitude in a much larger domain (ellipse). The images of the upper part (4m - 6m) of the aquifer are unreliable due to the presence of critically refracted waves at the groundwater table that are inverted as being transmitted waves. Compared to the ray-based inversion, the results from the full-waveform inversion show significantly higher resolution images at a depth of 6m-10m. Using existing petrophysical models, the inversion results and neutron-neutron logs are converted to porosity. Without any additional calibration, the values obtained for the converted neutron-neutron logs and permittivity results are very close and similar vertical variations can be observed [25].

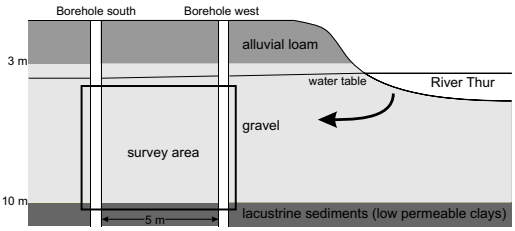

Fig. 5 Simplified geological representation of the investigation site showing a three-layer structure: alluvial loam, gravel, lacustrine (clay) sediments (from top to bottom). Boreholes close to the river Thur; water table -4m depth. After Klotzsche et al., 2010 [25].

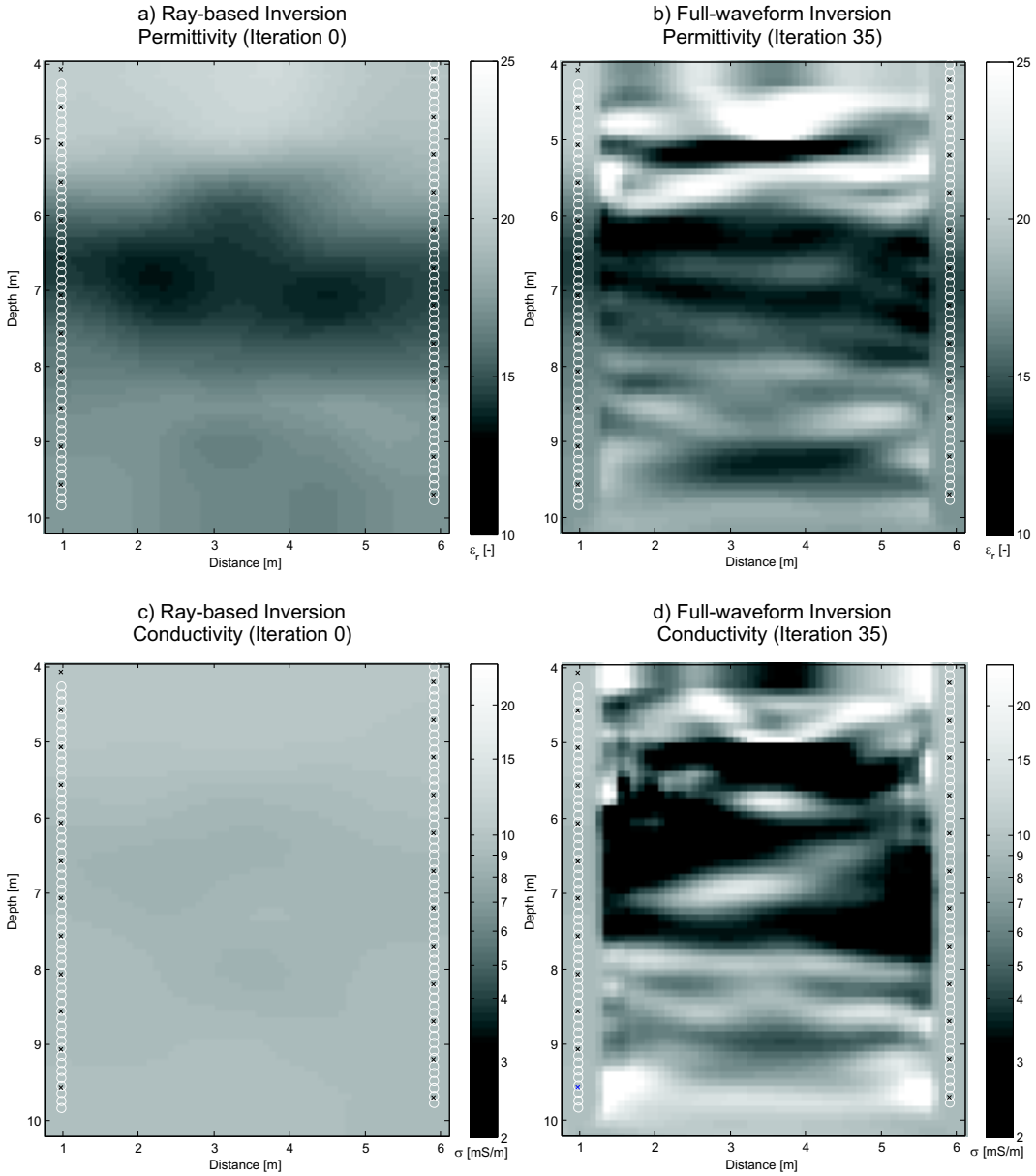

Fig. 6 Distribution of (a) relative permittivity and (c) conductivity from ray-based inversions that are used as the initial model for the full-waveform inversion,(b) permittivity and (d) conductivity tomograms for iteration 35. Transmitter and receiver positions are indicated with crosses and circles, respectively. After Klotzsche et al., 2010 [25].

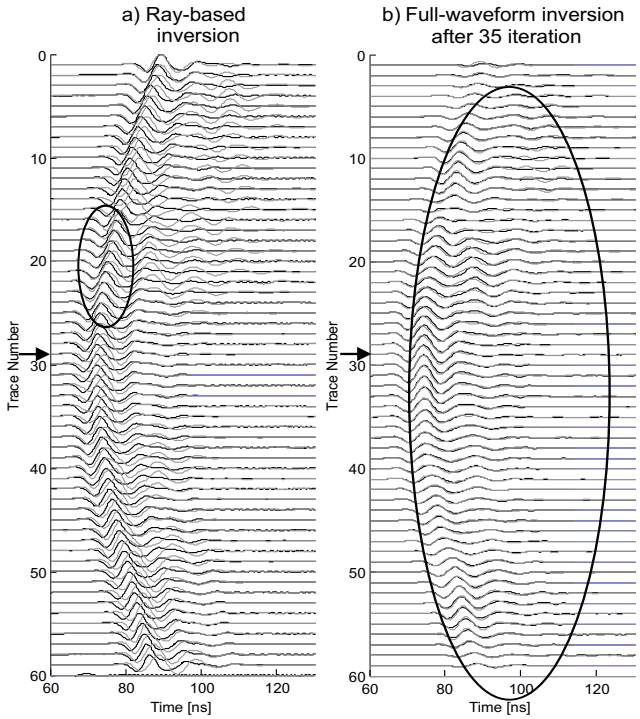

Fig. 7 Comparison of observed (gray) and synthetic (black) traces: (a) Ray-based inversion results using initial source wavelet (normalized), (b) results after the full-waveform inversion (iteration 35). The ellipses indicate the areas of best fit between the traces. The arrows at trace number 29 indicate location of the transmitter. After Klotzsche et al., 2010 [25].

5. CONCLUSIONS

We have shown three relatively new developments that return quantitative information from EMI and obtain sub-wavelength resolution in GPR images by correctly taking into account the electromagnetic wave propagation.

1) We have introduced a new calibration method for EM induction measurements using electrical resistivity tomography (ERT) inversion results. EM induction and ERT measurements were collected along a 120-metre-long transect. The inverted ERT data were used as input in an electromagnetic forward modeling tool for magnetic dipoles over a horizontally layered medium considering the frequencies and offsets used by the EM induction instruments. Comparison of the calculated and measured apparent electrical conductivities shows very similar trends but a clear shift in absolute values, which is attributed to system calibration problems. Calibration is carried out using linear regression that enables the quantitative mapping of apparent electrical conductivity values.

2) Shallow waveguide layers can be present due to large permittivity contrasts (e.g. due to precipitation, freezing or thawing events). GPR waves traveling in these shallow waveguides show clear dispersion. Reliable subsurface material properties can be obtained by calculating phase-velocity spectra, picking dispersion curves from the spectra and inverting for the medium properties using a combined global and local search algorithm. Here, the inversion algorithm includes the TE and TM reflection coefficients at the upper and lower interface of the waveguide.

3) We have applied a new full-waveform inversion scheme for GPR that includes the vectorial characteristics of the electric field and simultaneously inverts for permittivity and conductivity. The obtained images have a significantly higher resolution than conventional ray-based images. A remarkably good fit between the synthetic and measured traces is apparent for the phase and amplitude, which indicates an improved reconstruction of the medium properties within the subsurface.

ACKNOWLEDGMENTS

This work was supported by grants from ETH Zurich, the Swiss National Science Foundation and ETHs Competence Center for Environment and Sustainability (CCES). We thank the ETH Computer Services and the JSC in the research center Juelich for allowing us access the Brutus and Jump high performance clusters, respectively.

REFERENCES

[1] McNeill, J.D., Electromagnetic terrain conductivity measurements at low induction numbers, Geonics Technical Note, TN-6, 1980.

[2] Archie, G.E., The electrical resistivity log as an aid in determining some reservoir characteristics from bulk soil electrical conductivity in sandy soils, Transactions of the American Institute of Mining and Metallurgical Engineers, Vol. 146, pp. 54-61, 1942.

[3] Lavoué, F., van der Kruk, J., Rings, J.,André, F., Moghadas, D., Huisman, J.A., Lambot, S., Weihermüller, L., vanderBorght, J., and Vereecken, H., Electromagnetic induction calibration using electrical conductivity modeling based on electrical resistivity tomography, Near Surface Geophysics, Vol. 8, 3-11, 2010.

[4] Triantafilis, J., Laslett, G.M. and McBratney, A.B., Calibrating an electromagnetic induction instrument to measure salinity in soil under irrigated cotton, Soil Science Society of America Journal, Vol. 64, pp. 1009–1017, 2000.

[5] Sudduth, K.A., Drummond, S.T. and Kitchen, N.R., Accuracy issues in electromagnetic sensing of soil electrical conductivity for precision agriculture, Computers and Electronics in Agriculture, Vol. 31, pp. 239–264, 2001.

[6] Abdu, H., Robinson, D.A. and. Jones, S.B., Comparing bulk soil electrical conductivity determination using the DUALEM-1S and EM38-DD electromagnetic induction instruments, Soil Science Society of America Journal Vol. 71, pp. 189–196, 2007.

[7] Gebbers, R., Lück, E., Dabas, M. and Domsch, H., Comparison of instruments for geoelectrical soil mapping at the field scale, Near Surface Geophysics, Vol. 7, pp. 179–190, 2009.

[8] van der Kruk, J., Jacob, R.W., and Vereecken, H., Identifying dispersive GPR signals and inverting for surface waveguide properties, The Leading Edge, Vol. 28, pp. 936-940, 2009.

[9] van der Kruk, J., Properties of surface waveguides derived from inversion of fundamental and higher mode dispersive GPR data: IEEE Transactions on Geoscience and Remote Sensing, Vol. 44, pp. 2908-2915, 2006,

[10] van der Kruk, J., Streich, R., and Green, A. G., Properties of surface waveguides derived from separate and joint inversion of dispersive TE and TM GPR data, Geophysics, Vol. 71, pp. K19-K29, 2006.

[11] Arcone, S.A., Field observations of electromagnetic pulse propagation in dielectric slabs, Geophysics, Vol. 49, pp. 285-298, 1984.

[12] Liu, L., and Arcone, S. A., Numerical simulation of the wave-guide effect of the near surface thin layer on radar wave propagation, J. Environ. Eng. Geophysics, Vol. 8, pp. 133-141, 2003.

[13] Strobbia, C., and Cassiani, G, Multilayer ground-penetrating radar guided waves in shallow soil layers for estimating soil water content, Geophysics, Vol. 4, pp. J17-J29, 2007.

[14] van der Kruk, J., Steelman, C. M., Endres, A. L., and Vereecken, H., Dispersion inversion of electromagnetic pulse propagation within freezing and thawing soil waveguides: Geophysical Research Letters, Vol. 36, L18503, 2009.

[15] van der Kruk, J., Arcone, S. A., and Liu, L, Fundamental and higher order mode inversion of dispersed GPR waves propagating in an ice layer: IEEE Transactions on Geoscience and Remote Sensing, Vol. 45, pp. 2483-2491, 2007.

[16] Steelman, C.M., Endres, A.L., and van der Kruk, J., Field observations of shallow freeze and thaw processes using high-frequency ground-penetrating radar, Hydrological Processes, Vol. 24, pp. 2022-2033, 2010.

[17] Topp, G.C., Davis, J.L., Annan, A.P., Electromagnetic determination of soil water content: Measurements in coaxial transmission lines, Water Resources Research, 16, pp. 574-582, 1980.

[18] van der Kruk, J., Jacob, R.W., and Vereecken, H., Properties of precipitation-induced multilayer surface waveguides derived from inversion of dispersive TE and TM GPR data, Geophysics, Vol. 75, pp. WA263–WA273, 2010.

[19] Tarantola, A., A strategy for nonlinear elastic inversion of seismic-reflection data, Geophysics, vol. 51, pp. 1893-1903, 1986.

[20] Mora, P., Nonlinear two-dimensional elastic inversion of multioffset seismic data, Geophysics, Vol. 52, no. 9, pp. 1211-1228, 1987.

[21] Maurer, H., Greenhalgh, S.A., and Latzel, S., Frequency and spatial sampling strategies for crosshole seismic waveform spectral inversion experiments, Geophysics, Vol. 74, pp. WCC79-WCC89, 2009.

[22] Ernst, J.R., Maurer, H.R., Green, A.G., and Holliger, K., Full-waveform inversion of cross hole radar data based on 2-D finite-difference time-domain solutions of Maxwell's equations, IEEE Transactions on Geoscience and Remote Sensing, Vol. 45, pp. 2807-2828, 2007.

[23] Ernst, J.R., Green A.G. Maurer, H. and Holliger, K., Application of a new 2D time-domain full-waveform inversion scheme to crosshole radar data, Geophysics, 72, pp. J53-J64, 2007.

[24] Meles, G., van der Kruk, J., Greenhalgh, S.A., Ernst, J., Green, A.G. and Maurer, H., submitted, A new vector waveform inversion algorithm for simultaneous updating of conductivity and permittivity parameters from combination crosshole/Borehole-to-surface GPR data, IEEE Transactions on Geoscience and Remote Sensing, Vol. 48, pp 3391-3407, 2010.

[25] Klotzsche, A., van der Kruk, J., Meles, A.G., Doetsch, J., Maurer, H. and Linde, N., Full-waveform inversion of crosshole ground penetrating radar data to characterize a gravel aquifer close to the river Thur, Switzerland, Near Surface Geophysics, Vol. 8, pp 631-646, 2010.